

Comparison of 2-D and 3-D CFD simulations of bubbling fluidized beds with x-ray fluoroscopy and imaging experiments

Glenn Price¹, Blake Chandrasekaran², Ian Hulme³ and Apostolos Kantzas^{2,4}

1. NOVA Chemicals Research & Technology Centre, Calgary, Alberta, Canada
2. Department of Chemical Engineering, University of Calgary, Alberta, Canada
3. Rowan Williams Davies & Irwin Inc, Calgary, Alberta, Canada
4. Tomographic Imaging and Porous Media Laboratory, Calgary, Alberta, Canada

Computational Fluid Dynamics (CFD) is a promising tool for the development of comprehensive models of gas-phase polymerization in fluidized bed reactors. However, CFD models of gas-solids flow in fluidized beds are still under development and validation of these models on relatively simple test cases is essential if we hope to achieve reliable predictions of the complex phenomena associated with polyolefin production in commercial reactors. In the present study, numerical simulations of bubbling fluidized beds were performed in two (2-D) and three-dimensions (3-D) using the Eulerian granular multiphase model in Fluent, a commercial CFD package. The CFD simulation results are validated against experiments conducted on a small diameter, low-pressure fluidization column with ideal particles (glass beads with a narrow PSD). X-ray fluoroscopy and image processing techniques were applied to obtain detailed information about the bubbles in the bed, e.g. frequency distribution, bubble diameter and axial velocity. The 2-D simulations showed reasonably good agreement with the experimental bubble data on the coarse meshes but the predictions deviated as the mesh was refined. Next, a novel “numerical” x-ray technique was introduced to facilitate a direct comparison of the bubble properties from the 3-D CFD simulations with the x-ray based measurements. The 3-D bubble sizes and frequency data is well predicted using this approach but bubble velocities are significantly overpredicted by the 3-D simulations. Further work is needed to refine the numerical x-ray approach and the x-ray fluoroscopy based imaging technique.

1 INTRODUCTION

Since the introduction of the UNIPOL™ process by Union Carbide in 1968, gas-phase polymerization in fluidized bed (FB) reactors have become widely utilized for the commercial production of polyethylene and polypropylene. Given their importance in polyolefin production and many other industrial processes, it is not surprising that fluidized bed reactors have been the subject of much research over the past fifty years. Due to the tremendous increases in computing power, Computational Fluid Dynamics (CFD) is becoming an important tool to advance our understanding of the hydrodynamics in fluidized beds and ultimately may provide a means for the development of reliable, comprehensive models of commercial fluidized bed reactors [1]. From an industrial perspective, this sort of model would be invaluable to support the introduction of new high-performance catalysts, for design optimization and to troubleshoot problems on commercial gas-phase reactors.

While CFD is certainly a promising tool for the study of fluidized beds, the underlying models that are used to describe these gas-solid flows are still under development and

require extensive experimental validation. Direct numerical simulations of the particle motion and interstitial gas flow around the particles are well beyond existing computing capabilities. Even discrete particle models (DPM), where every particle in the bed is explicitly tracked in a Lagrangian manner are currently limited to relatively small number of particles ($<10^6$) [2]. Hence DPM is impractical for many fluidized bed problems as the beds typically contain a trillion particles or more depending on the application. Multi-phase continuum models [3-5] are well suited for simulating dense fluidized beds with a large number of particles because the particles are treated by statistical averaging over a region that is much larger than the particles. In this statistical treatment, the gas and solid particles are represented as fully interpenetrating continua with smoothly varying properties. Additional models are required for the constitutive relationships of the solids phase, which are usually derived by applying granular kinetic theory to account for the kinetic energy and slightly imperfect collision of the particles. The assumptions involved in the derivation of these models introduce uncertainty in simulation of gas-solids flows, analogous to the use of turbulence models in single-phase turbulent flow simulations. As a result, validation is a critical step in order to achieve reliable CFD predictions in the future.

The validation of multi-phase continuum models is an ongoing process, e.g. [2,6-8]. Most of the work in terms of fluidized beds has been mainly focused on freely bubbling fluidization of mono-dispersed Geldart-B type particles, although other fluidization regimes, e.g. slugging [8] and turbulent [9] have been examined. The predicted mean pressure drop and bed expansion are often compared with experimental measurements. Several researchers have compared the predicted pressure fluctuations at the wall with dynamic pressure measurements [6,10-11]. For instance, Wachem et al. [6] examined the simulated power spectral density of the pressure and voidage fluctuations, which they found matched correlations. More recently, Hulme [12] performed x-ray fluoroscopy experiments and used image processing to quantify the properties of bubbles generated in a bubbling fluidized bed. The measured bubble properties on the 3-D cylindrical column were compared with CFD simulations of a 2-D bed. Notwithstanding the validation efforts to date, most of the studies have been based on 2-D simulations using relatively coarse meshes. Mesh refinement studies, using a series of successively finer and finer meshes, are rare and there has been very little validation of 3-D simulations due to excessive computing requirements for a transient fluidized bed simulation with a large number of computational cells. Some exceptions may be found in references [9,11].

The main objective of the present study is to extend the validation of multi-phase continuum models by simulating dense fluidized beds using finer meshes in 2-D and to 3-D. Here the simulations are compared with the non-intrusive x-ray measurements of the detailed bubble information in a bubbling fluidized bed with ideal particles, i.e. spherical glass beads. A mesh refinement study was performed for the 2-D simulations in order to understand the implications of moving to finer meshes on the model predictions. A preliminary 3-D simulation of the fluidized bed was also performed to assess the differences in a 2-D and 3-D bed. A novel technique was developed to facilitate a more direct comparison of 3-D simulation results with x-ray imaging experiments. This is accomplished by simulating the passage of x-rays through the 3-D bed to generate a "numerical" x-ray image, which can be processed in a similar manner to the experimental images.

2 EXPERIMENTAL SETUP

Fluidization experiments were performed in a vertical plexiglass column. The straight section of the column has a constant diameter of 0.1 m and is 1 m in height. A disengagement zone is attached at the top of the straight section. The straight-section of the column is situated between an x-ray source and an image intensifier as illustrated in Figure 1. A porous plate distributor is located at the bottom of the column, which serves to contain the solid particles and uniformly distribute the air into the bed. A compressor is used to supply the airflow for the fluidization experiments at nearly atmospheric conditions. The flow rate of air is controlled and measured using a series of pressure regulators and rotameters. A cyclone downstream of the unit captures any solid particles that are entrained beyond the disengagement zone with the airflow out of the column. For this study, the experimental results were taken for ideal particles, glass beads with a narrow particle size distribution (150 to 250 μm) at a single superficial gas velocity ($2 U_{mf}$).

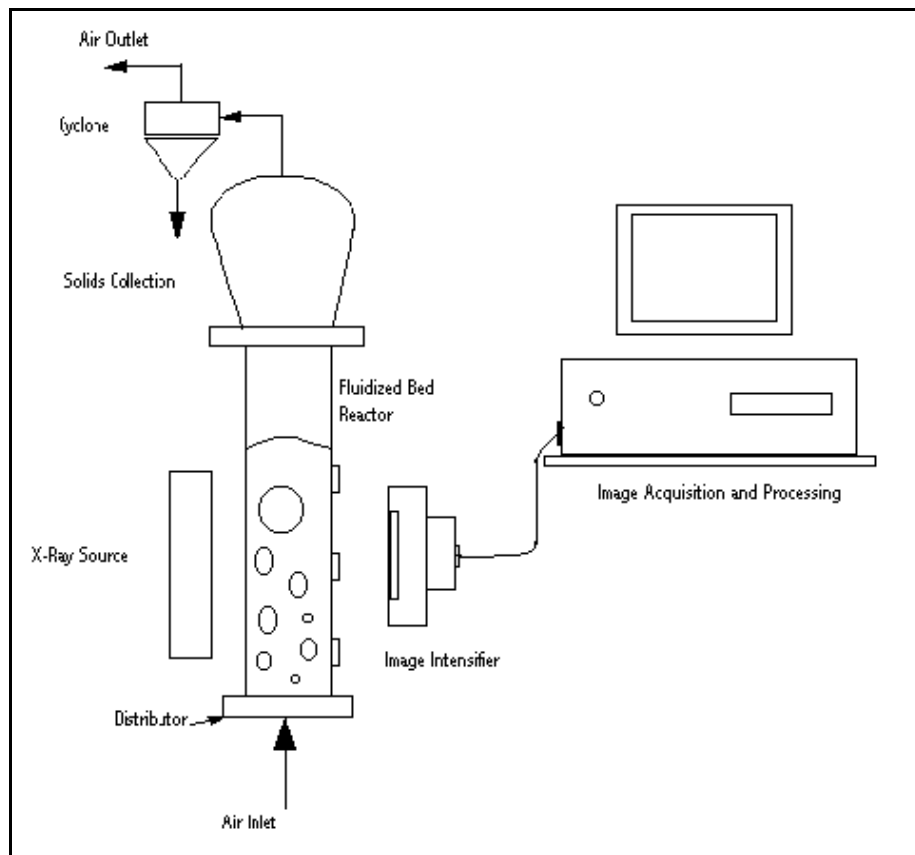


Figure 1: Schematic of experimental setup

2.1 X-ray Fluoroscopy

During an x-ray fluoroscopy experiment, x-rays emitted from the source pass through the column and are collected by an image intensifier. The x-rays are attenuated differently depending on the material that they pass through, which is the basis for capturing a bubble

image. While traditional x-ray radiography produces a single image, fluoroscopy can be used in conjunction with an image acquisition system to view moving objects. For the experiments used in this work, bubble images were acquired at a rate of 30 frames per second from the fluoroscopy unit using a frame grabber board (Matrox Meteor-II), which maintains maximum resolution. MeteorCapture Version 2.2 software was used to capture the images, which were stored on a computer for future processing. See Hulme [12] for a more complete description of the x-ray fluoroscopy measurements.

3 CFD SIMULATIONS

Numerical simulations of the fluidization experiments with glass beads were carried out in two- and three-dimensions using Fluent v6.1, a commercial CFD package [13]. The multi-phase continuum approach was invoked given the relatively large number of particles in the bed, $\sim 4.1 \times 10^8$. Only two fluids were employed here: a gas-phase to represent the air and a single solid phase to represent the nearly mono-dispersed glass beads. The gas-phase was treated as an incompressible fluid with constant transport properties. This is a reasonable assumption as the gas velocity in the bed is very small compared to the speed of sound and the total pressure drop across the bed is relatively low compared to the absolute pressure. The specified properties for the air and glass beads are summarized in Table 1 along with some of the other pertinent parameters that were used in the simulations.

Table 1: Input parameters for the CFD simulations

Description	Value	Comments
<u>Column Geometry</u>		
Diameter	0.1 m	Width for 2-D simulations
Height	1 m	
<u>Fluidized Bed</u>		
Initial bed height	0.4 m	
Initial solids packing	0.55	
Maximum solids packing	0.60	
<u>Gas Properties</u>		
Type	Air	
Density	1.21 kg/m ³	
Viscosity	1.8e-5 Pa.s	
<u>Particle Properties</u>		
Type	Glass beads	
Density	2480 kg/m ³	
Size	200 microns	
Coefficient of restitution	0.9	
Angle of internal friction	25°	
Minimum fluidization velocity	0.093 m/s	
<u>Process Conditions</u>		
Superficial gas velocity	0.186 m/s	~ 2 U _{mf}

3.1 Multi-Phase Continuum Model

The multi-phase continuum model in Fluent is based on a standard Eulerian-Eulerian treatment of the gas and granular solid phases. The gas and solid particles are considered to be separate but fully interpenetrating, continuous fluid phases. The solid or granular phase is represented as statistical ensemble of the particles based on the local solid particle concentration or volume fraction with effective set of particle properties. The solids phase has a separate velocity field from the gas phase. Governing conservation equations can also written for each phase and the equations are solved in an Eulerian framework.

By definition, the volume fraction of the gas and solid phases must sum to unity:

$$\varepsilon_g + \varepsilon_s = 1 \quad (1)$$

where ε_g and ε_s are the volume fractions of the gas and solid phases, respectively.

The conservation of mass for the gas is:

$$\frac{\partial}{\partial t} (\varepsilon_g \rho_g) + \nabla \cdot (\varepsilon_g \rho_g \vec{v}_g) = 0 \quad (2)$$

and the solid phase is:

$$\frac{\partial}{\partial t} (\epsilon_s \rho_s) + \nabla \cdot (\epsilon_s \rho_s \vec{v}_s) = 0 \quad (3)$$

where ρ_g and ρ_s are the density of the gas and solid phases, and \vec{v}_g and \vec{v}_s are the velocity vectors for the gas and solid phases.

The conservation of momentum can also written for the gas phase:

$$\frac{\partial}{\partial t} (\epsilon_g \rho_g \vec{v}_g) + \nabla \cdot (\epsilon_g \rho_g \vec{v}_g \vec{v}_g) = -\epsilon_g \nabla p + \nabla \cdot \overline{\overline{\tau}}_g + \epsilon_g \rho_g \vec{g} - \vec{F}_{gs} \quad (4)$$

and solid phase:

$$\frac{\partial}{\partial t} (\epsilon_s \rho_s \vec{v}_s) + \nabla \cdot (\epsilon_s \rho_s \vec{v}_s \vec{v}_s) = -\epsilon_s \nabla p - \nabla p_s + \nabla \cdot \overline{\overline{\tau}}_s + \epsilon_s \rho_s \vec{g} + \vec{F}_{gs} \quad (5)$$

where p is the gas static pressure, $\overline{\overline{\tau}}_g$ is the gas-phase stress tensor, \vec{F}_{gs} is the interaction force representing the momentum transfer between the two phases, and \vec{g} is the gravity acceleration vector. The granular pressure, p_s , and solid-phase stress tensor, $\overline{\overline{\tau}}_s$, are derived according to granular kinetic theory, which is based on an analogy between the random particle motion arising from particle-particle collisions and the thermal motion of gas molecules. Granular kinetic theory takes into account the inelasticity of the solid particle-particle collisions by means of an effective coefficient of restitution. An additional equation for the granular temperature of the solid phase, which represents the random fluctuations in kinetic energy resulting from particle collisions and velocity gradients, is also introduced by this theory. An algebraic form of the granular temperature equation is solved in Fluent v6.1. Finally, modifications are included to account for the elastic stresses generated in tightly packed solid regions by adopting theories from the study of soil mechanics.

Many different models of the constitutive relations for the solids stress tensor, solids collisional parameters and the momentum exchange between gas and solid phases are available in the literature. The pertinent models that were used in the present study are summarized in Table 2.

Table 2: Closure relations for two-phase continuum model.

Description	Model
Drag coefficient	Syamlal & O'Brien [19]
Granular shear viscosity	Gidaspow [5]
Granular bulk viscosity	Lun et al. [20]
Frictional viscosity	Schaeffer [21]
Solids pressure	Lun et al. [20]
Radial distribution function	Lun et al. [20]
Granular conductivity	Gidaspow [5]

3.2 Computational Domain

Transient numerical simulations of a bubbling fluidized bed require initial conditions as well as boundary conditions along the walls and at the inlet and outlet of the computational domain. The computation domain was selected to coincide with the vertical, constant-diameter section of the column above the porous distributor (see Figure 1). For the 2-D cases, the column was modeled as a rectangular plane in Cartesian coordinates as opposed to treating it as a 2-D axisymmetric problem. Other studies have shown that axisymmetric simulations predict symmetric, toroidal bubbles, which are not observed in real fluidized beds [12]. Here the full 3-D geometry of the experimental fluidization column was represented in the 3-D simulation.

3.3 Boundary & Initial Conditions

A uniform velocity profile for the gas equal to the superficial gas velocity (Table 1) was specified at the bottom of the domain. The solids volume fraction at the inlet was assumed to be zero at this location, i.e. there are no solid particles immediately above the distributor. The outlet at the top of the domain was treated as uniform pressure outlet assuming fully developed flow at this point. The walls of the column were assumed to be no-slip boundaries for both the gas and solid phases. At time $t = 0$, the column was assumed to be a loosely packed bed with an initial solids packing given in Table 1 and zero velocity field for both phases.

3.4 Numerical Treatment

Four different, uniform mesh sizes were employed in the 2-D simulations to assess the sensitivity of the results on the size of the computational cells. The total number of cells and the size of the cells in the different meshes are summarized in Table 3. Only a single mesh size was considered for the 3-D simulation due to the excessive computing requirements. The multi-block grid was developed for the 3-D simulation with more than 250k cells.

Table 3: Mesh sizes used for the CFD simulations.

Description	No. of cells	Cell size [cm]
2-D, mesh #1	1,000	1
2-D, mesh #2	4,000	0.5
2-D, mesh #3	16,000	0.25
2-D, mesh #4	64,000	0.125
3-D	257,280	0.3 (avg.)

Guenther & Syamlal [14] have shown that the use of a higher-order scheme with a compressive limiter (SUPERBEE) is essential to minimize smearing of the bubble boundaries. Hence, a bounded-version of QUICK was used for discretization of the convective terms in governing equations. This is the least diffusive scheme available in Fluent v6.1. A constant time step of 0.00025 s was maintained in all of the simulations. This value maintains the Courant number below unity even on the finest meshes. During a given time step, the convergence criteria for the residuals in the discrete equations was set to 1×10^{-4} . At this level of convergence, the relative change in the pressure at several monitored locations was less than 0.1%.

3.5 Image Output

The CFD simulations provide a great deal of information about the hydrodynamics of the bubbling fluidized bed. The local velocity and volume fraction of the gas and solid phases is provided in each computational cell along with additional particle variables such as the local granular pressure and granular temperature. The main variable of interest for the present purposes, however, is the local voidage or volume fraction of the gas phase, which is indicative of gas bubbles in the bed as the bubbles inherently contain less solid particles than in the surrounding bed.

For the 2-D simulations, a straightforward comparison can be made with the experimental x-ray images by plotting gray-scale contours of gas volume fraction over the rectangular domain at a rate of 30 frames per second. The situation is not as clear when comparing the 3-D simulation results. The simplest approach would be to plot contours of the gas volume fraction on a vertical slice plane through the center of the column. A center slice will not capture any bubbles away from this plane and bubbles can move in and out of the slice leading to bubble appearing and disappearing. Moreover, it does not provide a direct comparison with the x-ray fluoroscopy experiments. A more rigorous comparison is possible by replicating the x-ray passage and attenuation through the bed to obtain a final ensemble 2-D image. This sort of approach is used in the present work and the output is referred to as a “numerical x-ray” image.

Several different techniques could be used to generate a numerical x-ray image. Perhaps the best approach would be to utilize a ray-tracing algorithm to model the incident angle of the x-rays from the source anode and then track the attenuation and scattering of the x-rays as they pass through the column using voidage data from the 3-D CFD simulations. However, an alternate and much simpler approach is adopted here. Nineteen vertical slice planes are generated. These slices are evenly spaced across the cross-section of the column as shown in Figure 2. Each slice is a black and white image generated by a linear

mapping of the gas volume fraction to the gray scale (the gray scale used ranges from 0 – 255 for an 8-bit intensity image). Once the slice planes are generated, the numerical x-ray image is generated in the following manner:

1. Start at slice #1 with an initial x-ray intensity, I_o .
2. Convert the gray-scale value at each pixel in the image into a local gas voidage. This voidage is assumed to be constant over the fixed width, Δx , between slices.
3. Compute the attenuation of the x-ray as it passes through each pixel in the slice according to the Beer and Lambert relationship:

$$I = I_o \exp[-(\kappa_g \rho_g \varepsilon_g + \kappa_s \rho_s (1 - \varepsilon_g)) \Delta x] \quad (6)$$

where κ_g and κ_s are the x-ray mass attenuation coefficients for the gas and solid phases at the current x-ray intensity, I .

4. Move to the adjacent slice, i.e. slice #2, and repeat steps 2 and 3 until the x-rays pass through all of the slices sequentially up to slice #19.
5. Repeat steps 1-4 at the desired time step increment.

The x-ray mass attenuation coefficients were assumed to be constant during the analysis using values obtained from the NIST database [15] for glass and air at the peak energy of the x-rays generated in the experiments. The initial intensity of the x-ray beams was also adjusted to improve the contrast of the simulated image.

The image generated by this process is compared with gray-scale contours of gas voidage plotted on the center slice through the column (slice #10) in Figure 3. As might be expected, the numerical x-ray image is much blurrier than the contour plot but the same bubble shapes are apparent in both at this instant. The x-ray image is basically an ensemble of the bubbles in the column. At this time step, the center slice is a good representation of the bubble activity in the column. This is not always the case as will be shown later.

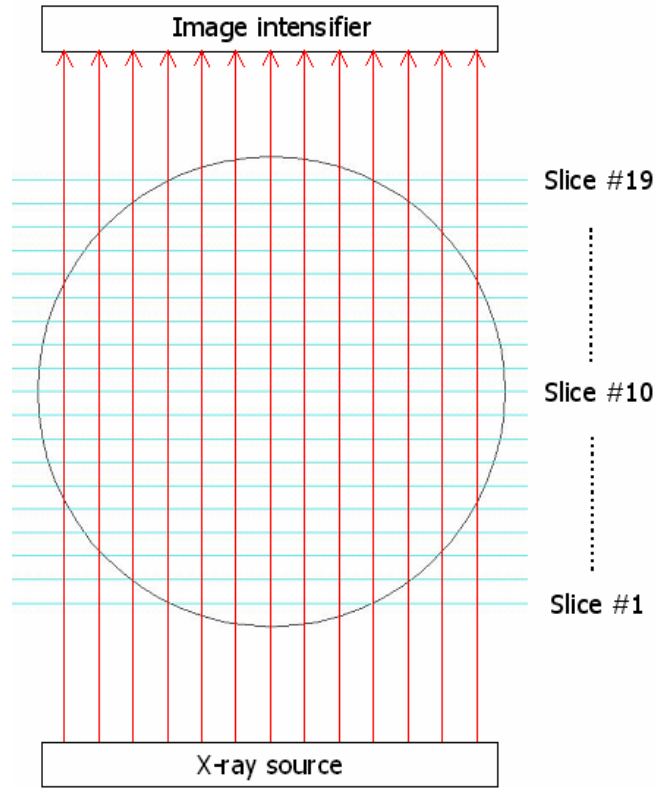


Figure 2: Location of vertical slices used in the generation of the “simulated” x-ray images.

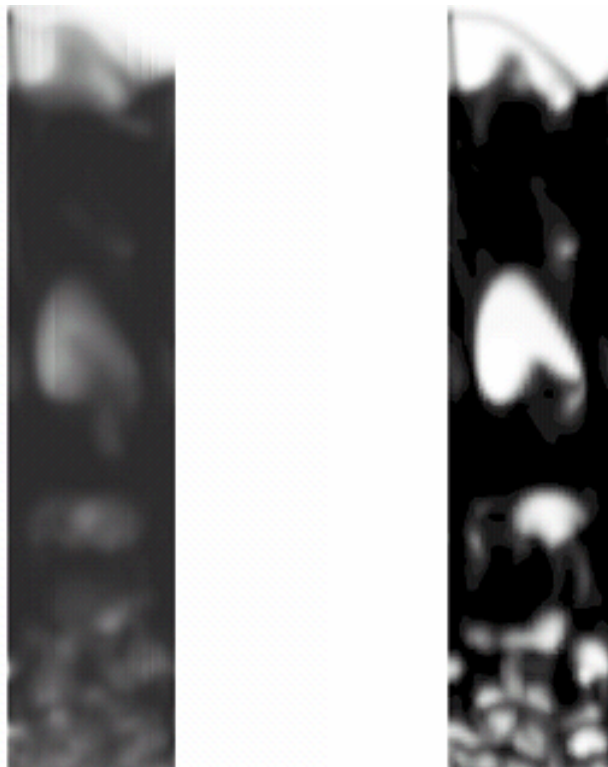


Figure 3: Comparison of “simulated” x-ray (left) with contour plot on center slice (right).

4 BUBBLE POST-PROCESSING

The collection of gray-scale images from the experiments and simulations need to be post-processed in order to obtain quantitative information about bubbles in the fluidized bed. This process essentially consist of three steps:

1. Image Processing
2. Bubble Identification
3. Bubble Tracking

4.1 Image Processing

The raw experimental and numerical images were first cropped to remove unwanted portions. As illustrated in Fig. 4, the raw experimental images are approximately 13.5 cm in diameter, which are then cropped into a 10 x 10 cm region. X-ray images were taken at four different heights to obtain a complete picture of the 40 cm fluidized bed in the column.

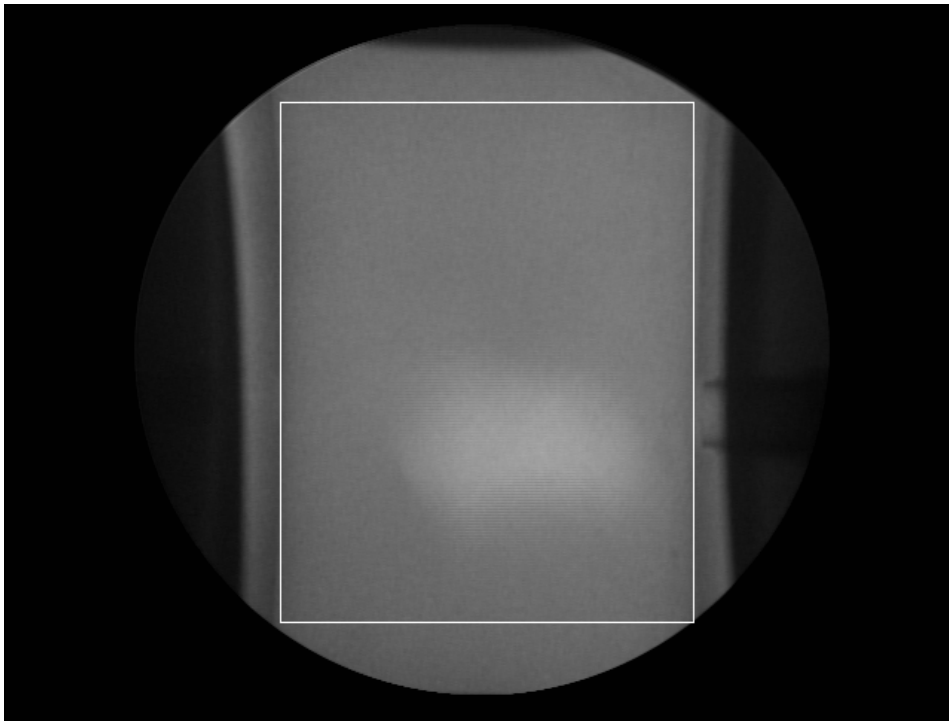


Figure 4: Raw image from the x-ray fluoroscopy unit showing the cropped window area that was used for image processing, Hulme [12]

Further processing of the cropped experimental images was necessary to address the following complications:

1. Background noise in the image caused by random radiographic noise and illumination effects.

2. Intensity bias due to the circular shape of the column, x-ray beam geometry and heeling effect. X-rays traveling through the side of the column will go through less material than the center. Hence, there will be a gradient from dark in the center to bright on the side.

The random noise in the experimental images was removed by using a simple filter based on the principle of neighborhood averaging. Specifically, a smoothing kernel was employed in which the smoothed pixel value is based on weighted average of the neighboring 3x3 block of pixel intensities around the central pixel. The bias in image intensity was corrected by performing a background subtraction. The background for this operation was obtained by averaging a certain number of frames. After the subtraction, opening and closing operations were performed to remove any speckling or holes in the image.

Note that with the exception of the numerical x-rays, typically the images from the CFD simulations should be devoid of these problems. However, the simulated images generated by FLUENT had artificially induced artifacts possibly due to a bug in the mapping program of FLUENT. To remove them first controlled morphological operations were applied to remove these artifacts and preserve the original image.

In the case of the numerical x-rays, a background subtraction, as in the experiments, was necessary in addition to the other steps for the other simulated images. The background subtraction was used to correct the intensity gradient introduced in the numerical x-ray images by the different x-ray path lengths through the circular geometry of the fluidized bed.

4.2 Bubble Identification

The bubble identification process is slightly different for the x-ray and simulated images. The x-ray images were segmented using a controlled local threshold instead of a constant global threshold as was done previously by Li [16]. This is done to overcome difficulties associated with differentiating between the larger and smaller bubbles in the column due to local intensity variations caused by the amount of material in the path of the x-ray beam [12]. A comparison of an experimental x-ray image before and after processing is shown in Figure 5.

Conversely, the simulated images are much cleaner and the bubbles can be identified using a global threshold. A global threshold corresponding to a void fraction of 0.8 was used for the present simulations. The simulations also provide a complete image of the fluidized bed, whereas the column was broken into four pieces during the experiments. An example of a cropped image from the simulations before and after a global threshold has been applied to obtain a binary image is illustrated in Figure 6.

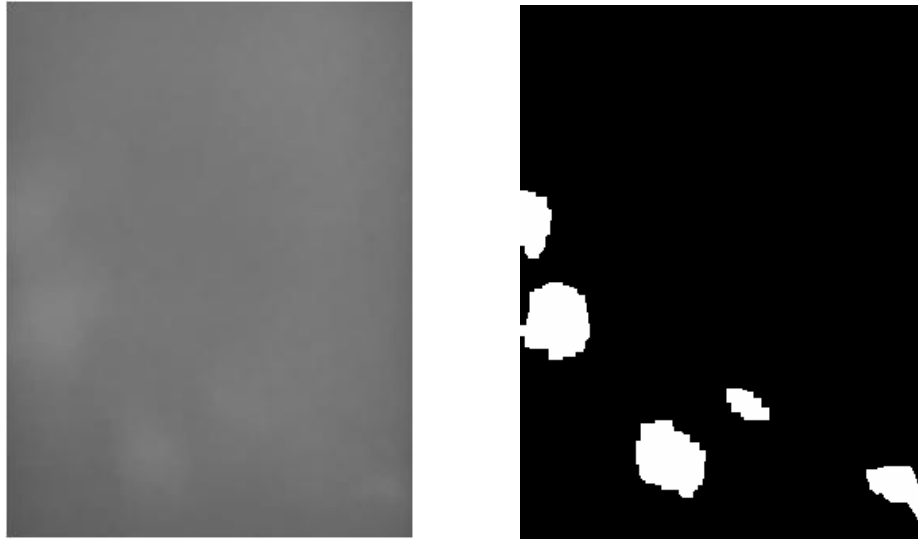


Fig. 5: The image on the left is the original cropped image from the x-ray fluoroscopy unit and the image on the right is the final image with the bubbles identified after image processing and local thresholding, Hulme [12].

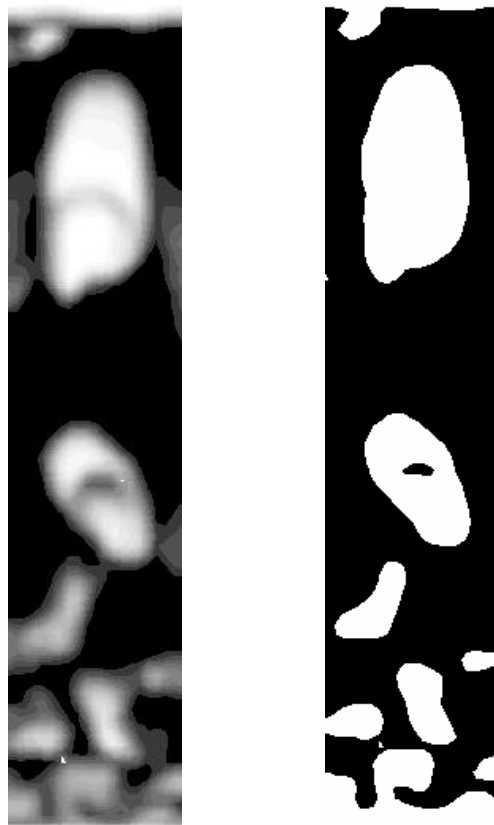


Fig. 6: Simulation images before and after thresholding and binarizing.

Once the bubbles have been identified, the effective bubble diameter can then be calculated based on the area of a circle that occupies the same area as that of the bubble. The effective diameter of an individual bubble, d_i , is:

$$d_i = \sqrt{\frac{4 \times (\text{Area of bubble})}{\pi}} \quad (7)$$

The individual bubbles are also labeled and their center of gravity is computed for bubble tracking purposes.

4.3 Bubble Tracking

Hulme [12] and Chandrasekaran [17] have developed an automated procedure for tracking the bubbles from frame to frame and computing their velocities. In the absence of coalescence and break-up, the bubbles can be matched between consecutive frames as they are labeled sequentially scanning from left to right and top to bottom. The axial and lateral velocity of the bubbles can be computed by comparing the change in the center of gravity in both directions based on the specified time step between frames. Of course problems arise when the bubbles coalesce, break-up, go out of the frame, come into the frame, or spontaneously appear and disappear. Therefore a set of rules and logic is required to properly identify each bubble from frame to frame. A complete description of the bubble-tracking algorithm is beyond the scope of this paper and interested readers should consult Chandrasekaran [17] for further details.

5 RESULTS AND DISCUSSION

5.1 Pressure Drop and Bed Expansion

The first step is to compare the predicted time-averaged pressure drop, ΔP , across the bed and the expanded bed height with the analogous data from the glass bead experiments. The time-averaged values from the CFD simulations and the experiments are summarized in Table 4 and Figure 7 respectively. Table 4 also includes the theoretical pressure drop based on the weight of the glass beads in the bed. The results show that the predicted ΔP from the 2-D and 3-D CFD simulations are in good agreement with the measured differential pressure across the bed.

However, the 2-D simulations tend to overestimate the time-averaged expansion of the fluidized bed by about 10% for the coarse mesh sizes (Other researchers, e.g. Gobin *et al.* [9], have reported similar results with 2-D simulations). The bed expansion decreases as the mesh is refined in 2-D and the bed expansion is over-predicted by about 5% on the finest mesh. The 3-D bed is slightly lower than the observed expansion but is within 3%. The reported decrease in bed height moving from 2-D to 3-D follows the same trend as Gobin *et al.* [9], who reported a 12% decrease; albeit these authors were comparing 2-D and 3-D simulation results for a turbulent fluidized bed, not a bubbling bed as was the case here.

Table 4: Comparison of the predicted pressured drop and expanded bed height with measured values from the experiment and theory.

	ΔP across the bed (Pa)
CFD, 2-D, mesh #1:	5055
CFD, 2-D, mesh #2:	5200
CFD, 2-D, mesh #3:	5210
CFD, 2-D, mesh #4:	5160
CFD, 3-D:	5250
Experiment:	5150 ± 100
Theoretical:	5350

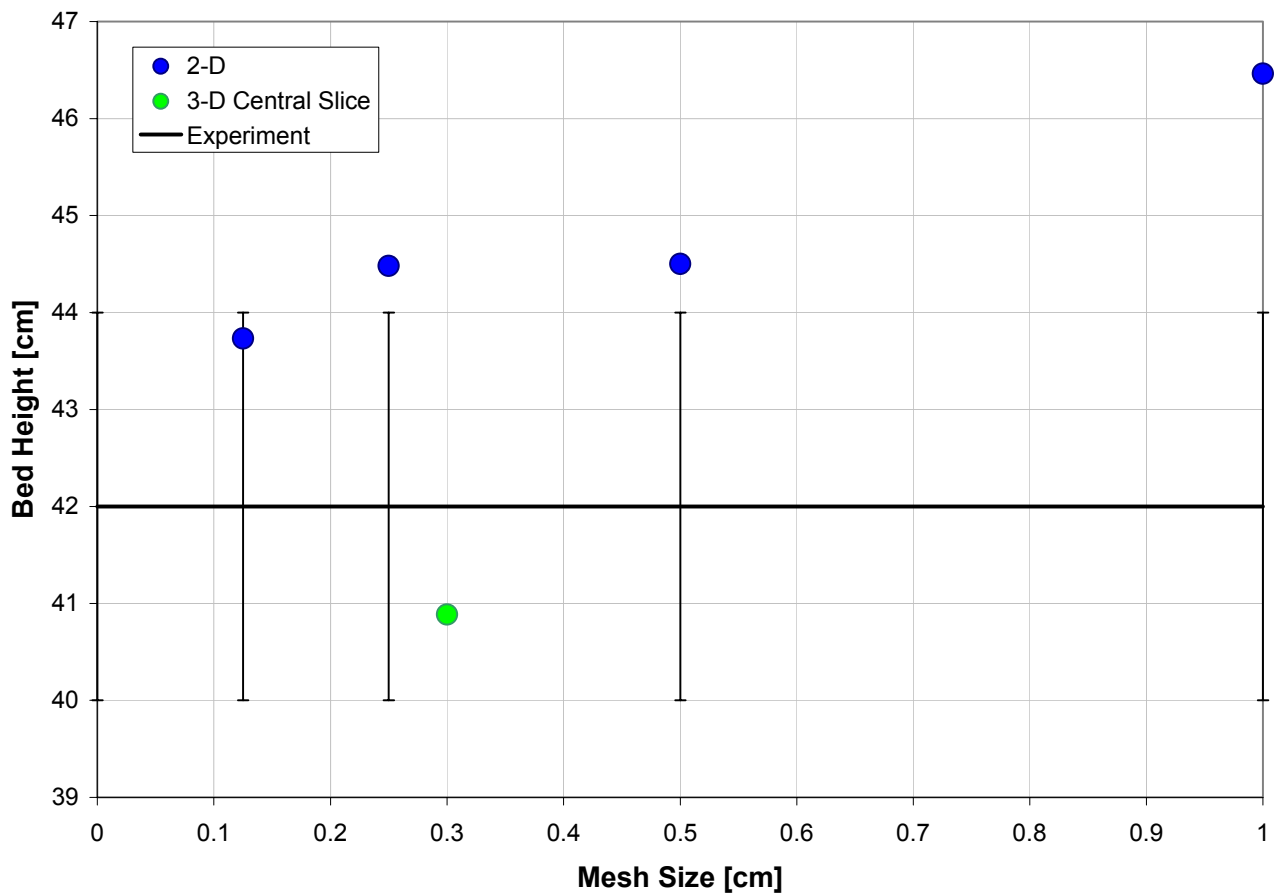


Figure 7: Effect of mesh size on expanded bed height.

5.2 Bubble Properties

5.2.1 2-D Simulation Results

The differences in the predicted gas bubbles from the 2-D simulations on the progressively finer mesh sizes are illustrated in Figure 8. The plotted contours of gas volume fraction for mesh #1 shows an excessive amount of smearing of the bubble boundaries. At this mesh resolution it is difficult to differentiate between individual bubbles in the bed. As expected, the bubble resolution improves dramatically as the mesh is refined. Individual bubbles are apparent on mesh #2, and the bubble boundaries are much sharper on even finer meshes. Even relatively small bubbles are resolved on mesh #4. This fact will become important when we examine the quantitative bubble statistics.

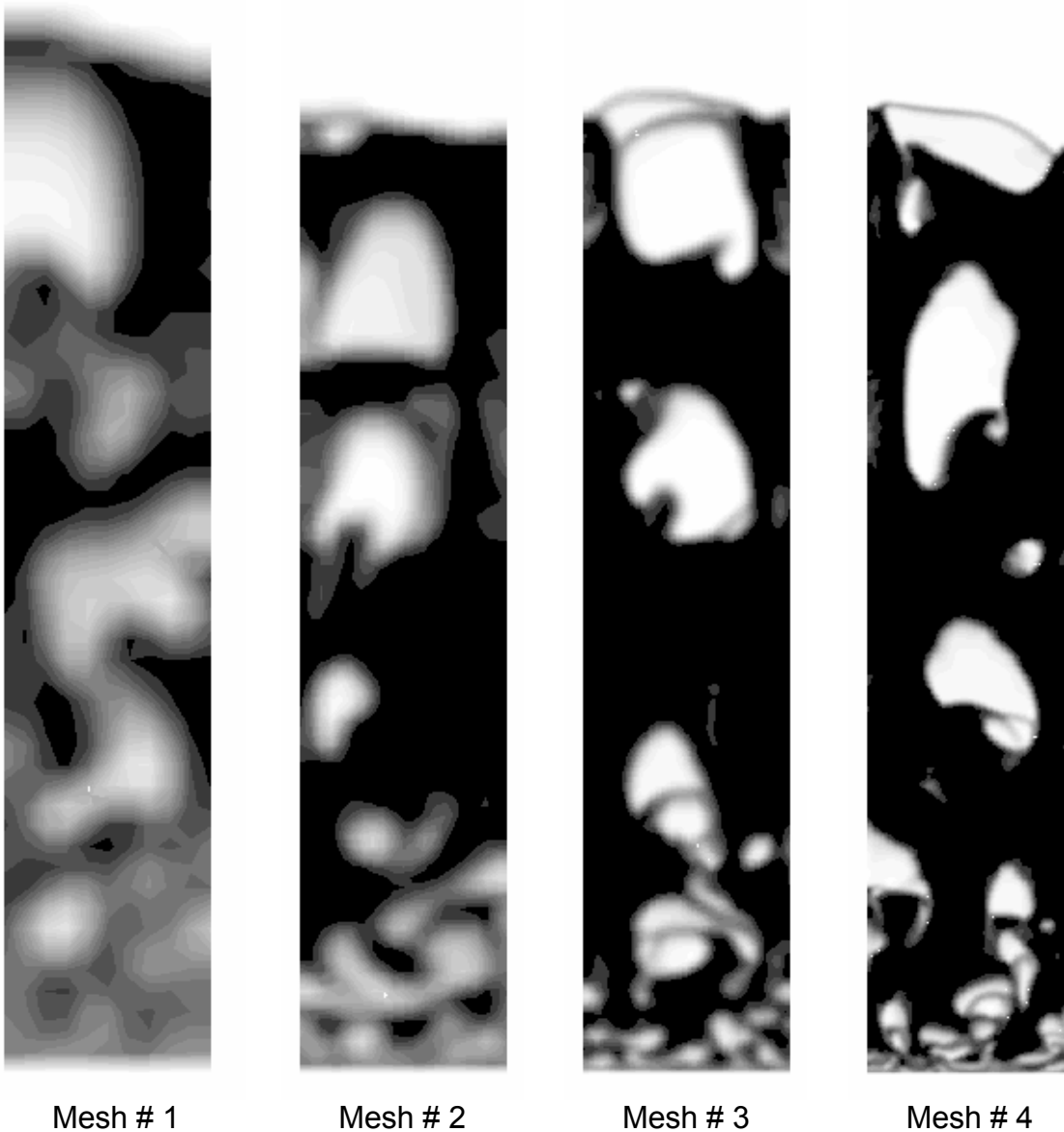


Figure 8: Effect of mesh size on the predicted gas bubbles in the bed.

Another observation that can be made from Figure 8 is that the bubbles are generally larger with increasing vertical distance from the distributor. A quantitative assessment of the bubble size as a function of height along bed is provided in Figure 9. For this figure the bubbles were identified and their sizes were computed in each frame as described previously in section 4. The arithmetic mean or number-averaged bubble diameter, \bar{d}_{10} :

$$\bar{d}_{10} = \frac{1}{n} \sum_{i=1}^n d_i \tag{8}$$

was calculated for the simulations by statistically averaging the bubbles contained in 4 cm bins along the length of the bed over a period of 30 seconds. A longer period was used for the experiments (~2 minutes). Tests have shown that 20 seconds is sufficient to reach almost stationary statistics.

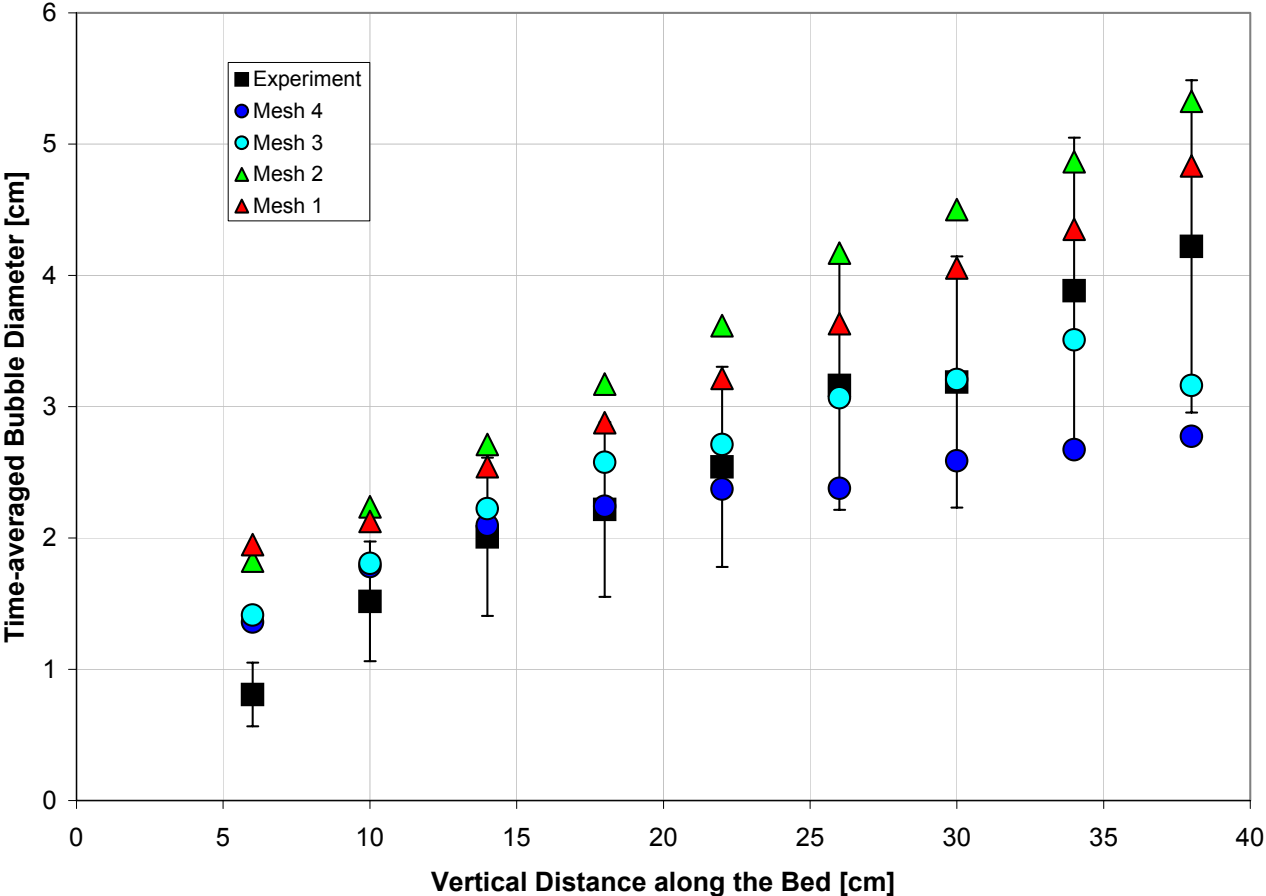


Figure 9: Effect of grid size on predicted bubble diameter vs. vertical distance along the bed. (2-D CFD simulations and experimental data).

As shown in Figure 9, the bubbles reach an average size of approximately 4 cm near the top of the bed based on the x-ray experiments. The predicted bubble diameters on the coarse meshes (mesh #1 and mesh #2) agree fairly well with the experiments in terms the slope of the bubble data, which is indicative of bubble growth with increasing vertical distance. The predictions start to deviate from the experimental data as the mesh is refined, however. The predicted bubble growth rate on mesh #3 is a little slower than the experiments but the predicted average bubble size is generally within the uncertainty of the measurements. Further mesh refinement, however, does not improve the accuracy of the prediction as shown by the mesh #4 results. Here the predicted bubble growth rate is much slower and the predicted average bubble diameter near the top of the bed is substantially smaller than the bubbles in the x-ray imaging experiments.

Looking back at the bubble images in Figure 8, one might wonder why the predicted average bubble diameter is so small in the mesh #4 simulation when there is clearly a large bubble present near the top of the bed (at least for this given instant in time). The reason can be found by examining the frequency distribution of the bubble sizes in the bed (Figure 10) as well as the frequency distribution at a specified height of 34 cm near the top of the bed (Figure 11). From these figures it is clear that none of the 2-D simulations agree particularly well with the experimental bubble frequency data. The coarsest mesh yields an excessive number of 3.3 cm bubbles in the bed, but agrees surprisingly well with the experimental data near the top of the bed. Mesh #2 agrees fairly well in terms of the overall bubble sizes in the bed but tends to overpredict the number of large bubbles at 34 cm. The finer mesh results show a shift in the bubble frequency towards the smaller bubble sizes. There are a much larger number of small bubbles in bed according to simulations. This results in a bi-modal distribution near the top of the bed with lots of small bubbles along with some very large bubbles (~6-7 cm). The experiments only show a unimodal distribution in bubbles sizes at 34 cm.

There are several possible causes for this discrepancy. First, it is very difficult to identify small, individual bubbles from the x-ray images as the change in x-ray attenuation is difficult to detect. Therefore, small bubbles might be present in the actual column but they were not detected during the image processing. Second, there could be a problem with the models that were selected to represent the solids stresses for the granular phase. Or it could be that the granular kinetic theory itself is incapable of accurately predicting the detailed bubble properties under these conditions. The fine mesh solutions have less numerical diffusion, and a lower artificial viscosity than the coarser meshes. Thus, the effective viscosity in the packed granular media surrounding the bubbles in the fine mesh simulations is lower than the coarser meshes, and possibly lower than in reality as a viscous media will likely lead to less bubble break-up. Finally, the discrepancy could be related to a fundamental difference in the bubble formation in a 2-D bed vs. a 3-D circular column. The latter hypothesis can be validated by the 3-D simulation results.

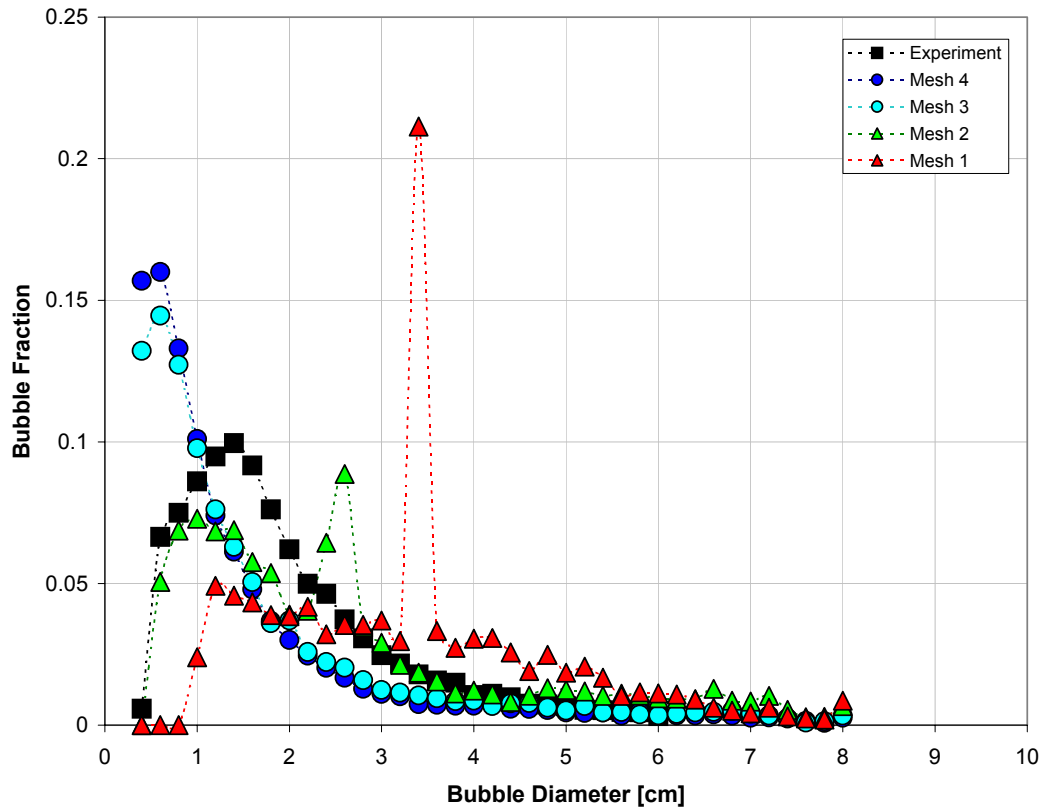


Figure 10: Frequency distribution of bubble diameters in the entire bed.

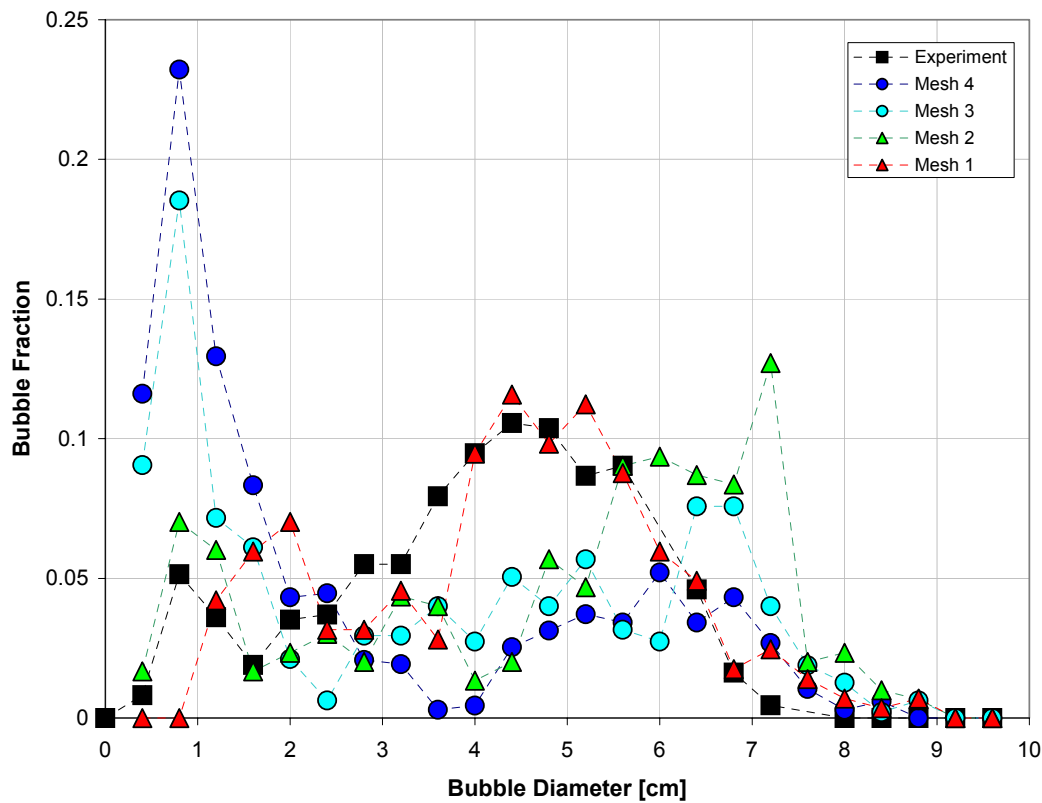


Figure 11: Frequency distribution of bubble diameters at a vertical distance of 34 cm.

Another important consideration is the vertical (upwards) velocity of the bubbles in the beds. The predicted time-averaged axial velocity of the bubbles is compared to the axial bubble velocities from the x-ray imaging experiments in Figure 12. Generally speaking, the velocity results are consistent with the bubble diameter data. The coarser meshes (mesh #1 and #2) generally overpredict the bubble velocity near the top of the bed compared to the experimental values. The average bubble velocity results on mesh #3 are fairly close to the experiments, which is reasonable to expect given that average bubble diameters are also similar (Figure 9). The fine mesh #4 simulation once again underpredicts the bubble velocities near the top of the bed presumably because the bubbles are smaller than the experiments. However, all of the 2-D predictions are within the uncertainty of experimental bubble velocity data.

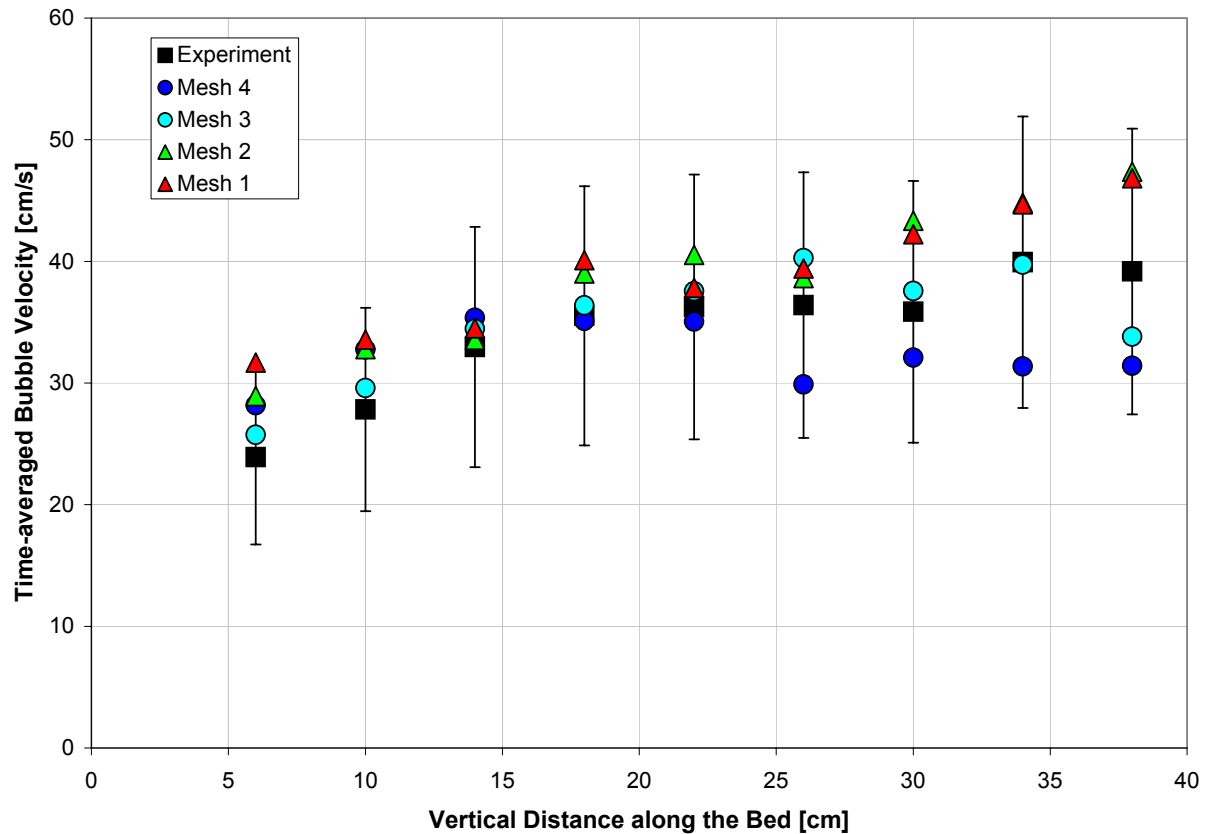


Figure 12: Average bubble upward velocity vs. vertical distance along the bed.

5.2.2 3-D Simulation Results

A single 3-D simulation of the bubbling glass beads fluidized bed was run for 80,000 time steps to provide 20 s of simulated time. The single run took almost 20 days of CPU time using Fluent v6.1 in parallel on 20 - 3.4 GHz Intel P4s. Only 12 s of simulated run time was available for image processing after discarding the first 8 s to eliminate the transient effects associated with start-up of the fluidization process. The numerical x-ray images were generated as described in section 3.5 and the resulting bubble properties are compared with the results for a single vertical slice through the center of the column.

The predicted time-averaged bubble diameters along the length of the bed are compared with the experimental values in Figure 13. Except at the bottom of bed, both the center slice and the numerical x-ray predictions are in good agreement with the measured bubble diameters along the length of the bed. Unlike the center slice, however, the numerical x-ray captures the bubbles away from the center of the column. This leads to a slightly smaller bubble diameter than the center slice approach as the off center bubbles are generally smaller as illustrated in Figure 14. The large, 3-D bubbles near the center of the column can also be larger than the portion that cuts through the center plane.

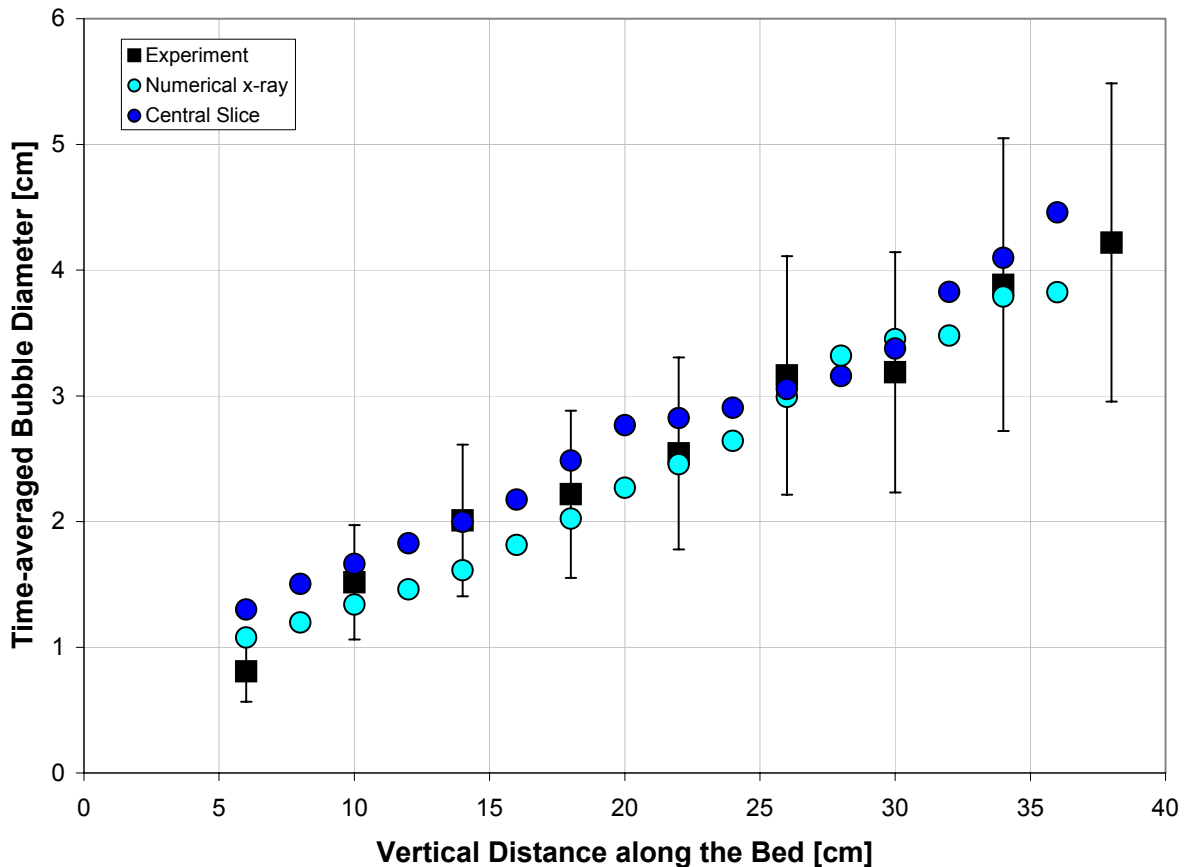


Figure 13: Predicted average bubble diameter vs. vertical distance along the bed. (3-D CFD simulations and experimental data)

The predicted and experimental frequency distribution of bubbles in the entire bed and at a vertical height of 34 cm in the bed is presented in Figures 15 and 16, respectively. Generally speaking, the 3-D prediction is in much better agreement with the measured bubble frequency data than the 2-D simulations (compare Figures 15 & 16 with Figures 10 & 11). The 3-D CFD simulations predict more small-diameter bubbles than were captured during x-ray imaging experiments as indicated by the bubble frequency plots (Figures 15 & 16); though not as many as the 2-D fine mesh simulations (Figures 10 & 11). It is difficult to say based on a single 3-D simulation, however, whether this is a true property of the 3-D bed as the 3-D mesh density was coarser than the fine 2-D meshes and only 12 s of data was processed vs. 30 s in 2-D.

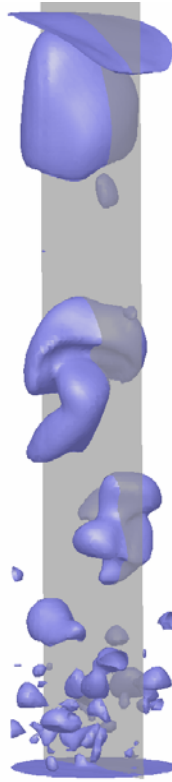


Figure 14: Predicted 3-D bubble shapes in the bed at a snapshot in time. The central slice is also shown to illustrate the number of bubbles not captured on this plane.

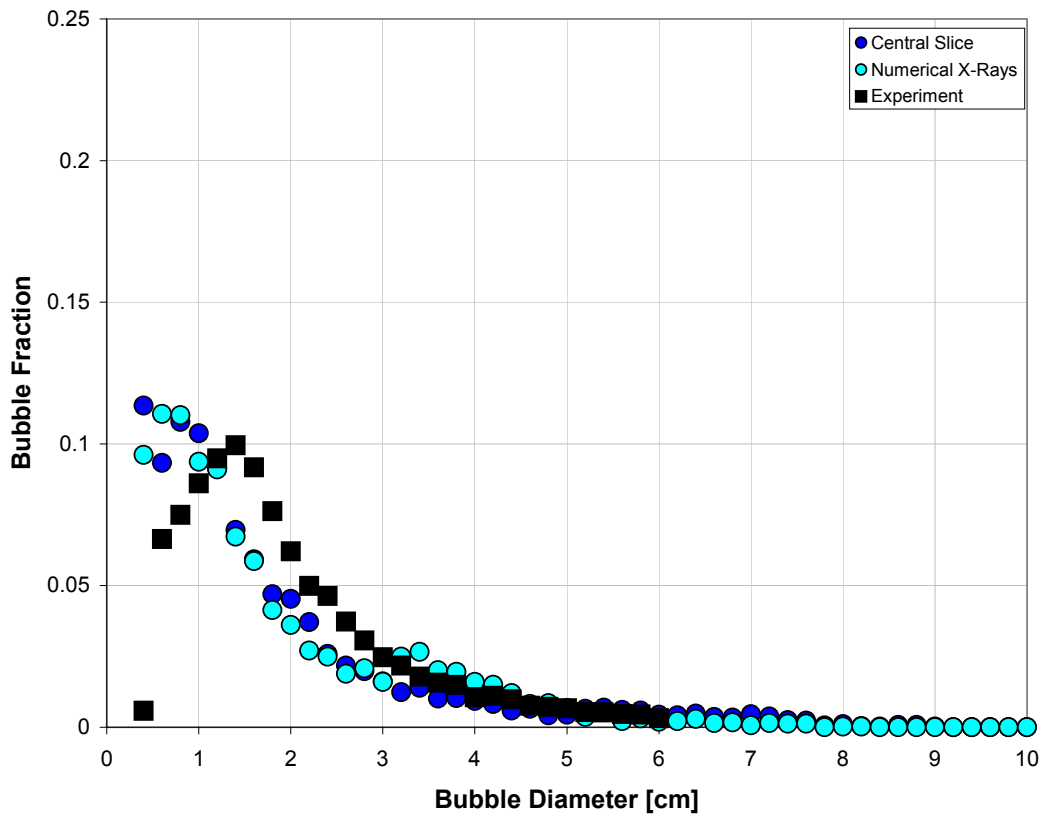


Figure 15: Frequency distribution of bubble diameters in the entire bed (3-D simulations).

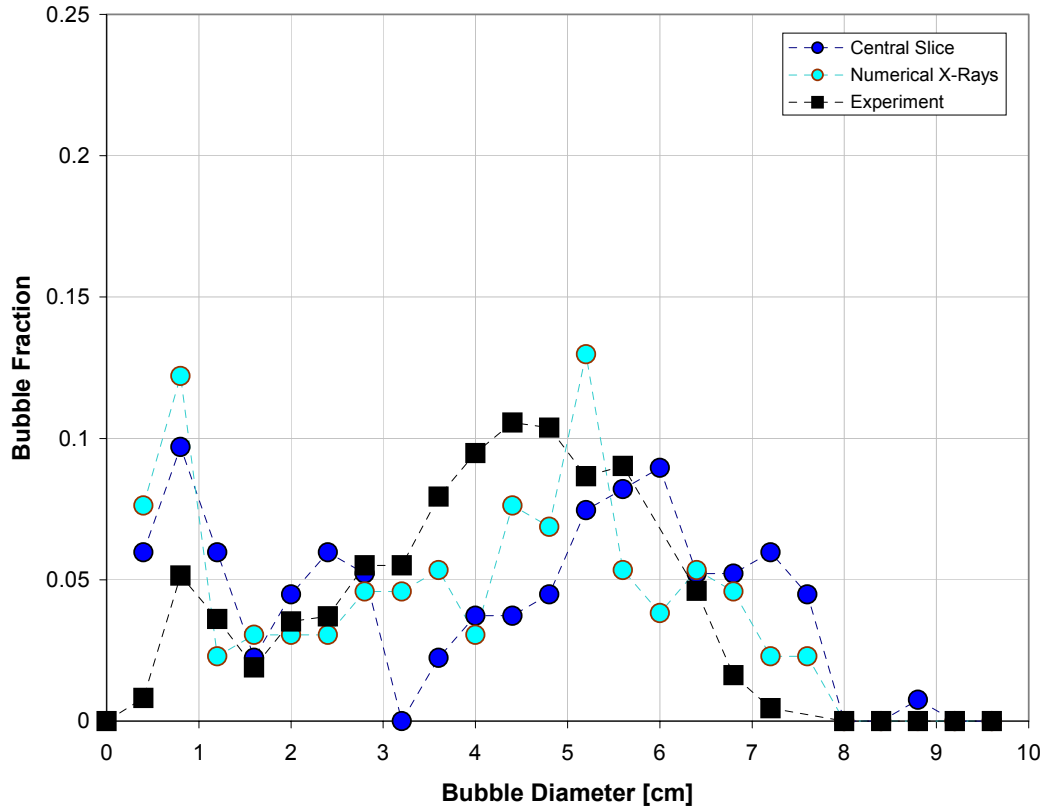


Figure 16: Frequency distribution of bubble diameters at a vertical distance of 34 cm (3-D simulations vs. experiments)

Finally the predicted average upward velocity of the bubbles along the length of bed is plotted vs. vertical distance along the bed in Figure 17. Given the good agreement in terms of bubble sizes, it is surprising that the 3-D simulations substantially overpredict the velocity of the bubbles compared to measured data (especially since the 2-D simulations did a good job in this regard). However, the rise velocity of a 3-D (spherical) bubble is theoretically different than the rise velocity of a 2-D (cylindrical) bubble due to the different surface-to-volume ratio for these different shapes [18]. The drag on the bubbles is proportional to their surface area, while the buoyancy force is proportional to the volume of the bubble. Nevertheless, the velocity discrepancy cannot be explained away in this manner because the 3-D simulations should match the experimental bubble behavior not the 2-D data. Further work is needed to elucidate the source of this discrepancy including a critical look at the experimental velocity data.

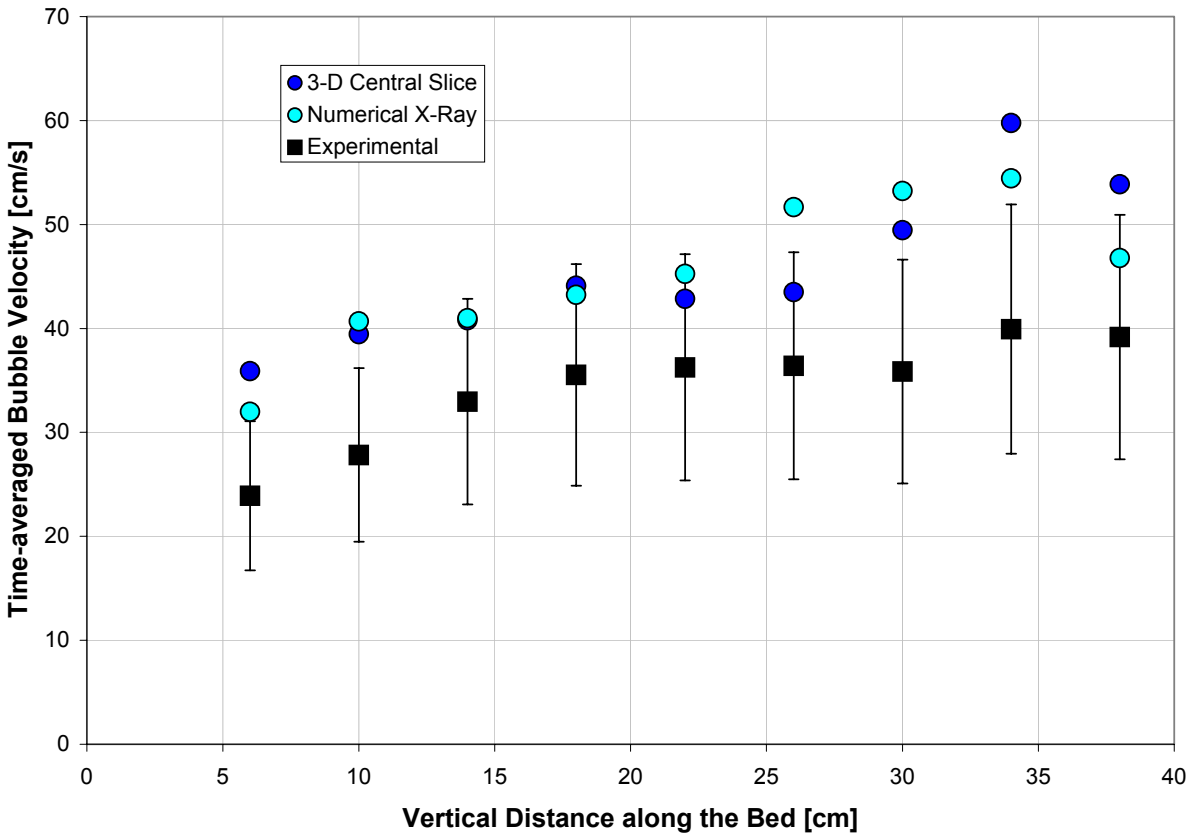


Figure 17: Average bubble upward velocity vs. vertical distance along the bed.

6 CONCLUSIONS AND RECOMMENDATIONS

The predicted bubble properties from 2-D and 3-D CFD simulations of a bubbling fluidized bed were compared with detailed data from x-ray fluoroscopy experiments and image processing. The 2-D results are interesting in the sense that reasonably good agreement was achieved with the experimental data on fairly coarse meshes. Hence, one could be easily fooled into thinking that the CFD model has been validated on the basis of this comparison alone. However, a 2-D mesh refinement study has shown that the CFD predictions deviate from the experimental results due to a larger fraction of small bubbles that are generated on successively finer meshes. At this point, it is unclear whether this is the true behavior of 2-D bed but care should be taken when relying coarse mesh simulations of fluidized beds for validation purposes.

A single 3-D simulation of the fluidized bed showed much better agreement with the experimental bubble data in terms of the average bubble size and frequency distribution of bubbles. However, the velocity of the bubbles was substantially overpredicted compared to measured values along the length of the bed and 2-D simulations. The 3-D bubble velocities should theoretically differ from the 2-D prediction due to the different surface-to-volume ratio for 3-D bubbles vs. 2-D cylindrical bubbles. Additional work is needed to fully

explain the discrepancy between the 3-D simulations and the measured bubble velocity data.

Finally, a new technique is proposed that provides for a more direct comparison of the 3-D simulation results with the x-ray imaging experiments. Instead of simply plotting the predicted contours of gas voidage on a vertical slice through the center of the column, a numerical x-ray image is generated based on calculating the attenuation of virtual x-rays as they pass through the 3-D bed. Although there was not much difference between the numerical x-rays and the center slice results on this small-diameter column, numerical x-rays may prove to be more useful on larger-diameter beds. Additional work is also needed to improve the numerical x-ray method and the x-ray fluoroscopy based imaging technique. Finally, more 3-D simulations and experiments are needed on larger-diameter columns using ideal and non-ideal particles to further advance the validation of multi-phase continuum models on dense fluidized beds.

7 ACKNOWLEDGEMENTS

We would like to acknowledge the Natural Sciences and Engineering Research Council of Canada (NSERC), the Canada Research Chair in Energy and Imaging and NOVA Chemicals Corporation for providing financial support for this work. We would also like to thank Dr. Kamal Botros, Eric Clavelle, Jonathan O'Brien and Mohammad Shariati for valuable discussions during the course of this study and for reviewing this manuscript. Permission to publish this paper by NOVA Chemicals Corporation is also hereby acknowledged.

REFERENCES

1. Fan, R., D.L. Marchisio and R.O. Fox, "CFD simulation of polydisperse fluidized bed polymerization reactors", submitted to *AIChE Symposium Series*, 2003.
2. Goldschmidt, M.J.V, R. Beetstra and J.A.M. Kuipers, "Hydrodynamic modeling of dense gas-fluidized bed: comparison and validation of 3D discrete particle and continuum models", *Powder Technology*, **142**, pp.23-47, 2004.
3. Ding, J. and D. Gidaspow; "A bubbling fluidization model using kinetic theory of granular flow", *AIChE Journal*, **36**, pp.523-538, 1990.
4. Syamlal, M., Rogers, W. & O'Brien, T.J., *MFIX Documentation: Theory Guide*, U.S. Department of Energy, DOE/METC-94/1004, 1993.
5. Gidaspow, D.; *Multiphase Flow and Fluidization*, Academic Press, Boston, 1994.
6. van Wachem, B.G, J.C. Schouten, R. Krishna and C.M. van den Bleek, "Validation of the Eulerian simulated dynamic behavior of gas-solid fluidized beds", *Chemical Engineering Science*, **54**, pp.2141-2149, 1999.

7. Boemer, A., H. Qui and U. Renz; "Verification of Eulerian simulations of spontaneous bubble formation in a fluidized bed", *Chemical Engineering Science*, **53**, pp.1835-1846, 1998.
8. Lettieri, P., L. Cammarata, G. Micale and J. Yates, "CFD simulation of gas fluidized beds using alternative Eulerian-Eulerian modeling approaches", *International Journal of Chemical Reactor Engineering*, **1**, 2003.
9. Gobin, A., H. Neau, O. Simonin, J. Llinas, V. Reiling and J. Selo; "Numerical simulation of a gas phase polymerization reactor", *European Congress on Computational Methods in Applied Sciences and Engineering (ECCOMAS) Computational Fluid Dynamics Conference*, Wales, 2002.
10. Ding, J. and S. Tam; "Asymptotic power spectrum analysis of chaotic behaviour in fluidized beds", *International Journal of Bifurcation & Chaos*, **4**, pp.327-341, 1994.
11. Peirano, E., V. Delloume and B. Leckner, "Two- or three dimensional simulations of turbulent gas-solid flows applied to fluidization", *Chemical Engineering Science*, **56**, pp.4787-4799, 2001.
12. Hulme, I.; *Verification of the Hydrodynamics of a Polyethylene Fluidized Bed Reactor using CFD and Imaging Experiments*, Masters Thesis in Chemical Engineering, University of Calgary, 2003.
13. *Fluent v6.1 User's Manual*, Fluent Inc., Lebanon, N.H., 2003.
14. Guenther, C. and M. Syamlal; "The effect of numerical diffusion on isolated bubbles in a gas-solids fluidized bed", *Powder Technology*, **116**, pp.142-154, 2001.
15. NIST Physical Reference Data, Tables of X-Ray Mass Attenuation Coefficients, <http://physics.nist.gov/PhysRefData/XrayMassCoef/cover.html>.
16. Li, F.; *Study of Bubble Flow in Fluidized Beds*, Masters Thesis in Chemical Engineering, University of Calgary, 1999.
17. Chandrasekaran, B.; "A validation study of the computed hydrodynamics of a gas-solid fluidized bed", Masters Thesis in Chemical Engineering, University of Calgary, 2004..
18. Davidson, J.F. and D. Harrison; *Fluidized Particles*, Cambridge University Press, New York, 1963.
19. Syamlal, M. and T.J. O'Brien; "Computer simulation of bubbles in a fluidized bed", *AIChE Symposium Series*, **85(27)**, pp.22-31, 1989.
20. Lun, C., S.B. Savage, D. Jeffrey and N. Chepurnity, "Kinetic theories for granular flow: inelastic particles in Couette flow and slightly inelastic particles particles in a general flow field", *Journal of Fluid Mechanics*, **140**, pp.233-256, 1984.

21. Schaeffer, D.; "Instability in the evolution equations describing incompressible granular flow", J. Diff. Eq., **66**, pp.19-50, 1987.

NOMENCLATURE

d_i	effective diameter of an individual bubble
\bar{d}_{10}	arithmetic or number-averaged bubble diameter
\vec{F}_{gs}	interaction force between the gas and solid phase
\vec{g}	gravity acceleration vector
p	gas static pressure
p_s	granular pressure
t	time
U_{mf}	superficial gas velocity at minimum fluidization
\vec{v}_g	velocity vector for the gas phase
\vec{v}_s	velocity vector for the solids phase

Greek Letters:

ε_g	volume fraction of the gas phase
ε_s	volume fraction of the solids phase
ρ_g	density of the gas phase
ρ_s	density of the solids phase
$\overline{\tau}_g$	stress tensor for the gas phase
$\overline{\tau}_s$	stress tensor for the solids phase